



HAL
open science

Three-dimensional and high-resolution building energy simulation applied to phase change materials in a passive solar room

Teddy Gresse, Lucie Merlier, Jean-Jacques Roux, Frédéric Kuznik

► To cite this version:

Teddy Gresse, Lucie Merlier, Jean-Jacques Roux, Frédéric Kuznik. Three-dimensional and high-resolution building energy simulation applied to phase change materials in a passive solar room. *Energy and Buildings*, 2022, 274, pp.112418. 10.1016/j.enbuild.2022.112418 . hal-04259408

HAL Id: hal-04259408

<https://hal.science/hal-04259408>

Submitted on 26 Oct 2023

HAL is a multi-disciplinary open access archive for the deposit and dissemination of scientific research documents, whether they are published or not. The documents may come from teaching and research institutions in France or abroad, or from public or private research centers.

L'archive ouverte pluridisciplinaire **HAL**, est destinée au dépôt et à la diffusion de documents scientifiques de niveau recherche, publiés ou non, émanant des établissements d'enseignement et de recherche français ou étrangers, des laboratoires publics ou privés.

Highlights

Three-dimensional and high-resolution building energy simulation applied to phase change materials in a passive solar room

Teddy Gresse, Lucie Merlier, Jean-Jacques Roux, Frédéric Kuznik

- Three-dimensional, high-resolution dynamic thermal modeling of a PCM-integrated room.
- Model was validated using experimental data.
- Investigated PCM-integrated building walls during summer.
- PCM significantly reduced the peak surface temperature and temperature fluctuations.
- PCM integration could be limited to the sun patch trajectory.

Three-dimensional and high-resolution building energy simulation applied to phase change materials in a passive solar room

Teddy Gresse^{a,*}, Lucie Merlier^b, Jean-Jacques Roux^a, Frédéric Kuznik^a

^a*Univ Lyon, INSA Lyon, CNRS, CETHIL, UMR5008, Villeurbanne, F-69621, France*

^b*Univ Lyon, UCBL, INSA Lyon, CNRS, CETHIL, UMR5008, Villeurbanne, F-69621, France*

Abstract

Phase change materials (PCMs) reduce energy consumption and improve indoor thermal comfort in buildings. Various numerical models have been developed to evaluate the thermal performance of the PCMs integrated into building enclosures. To remain computationally efficient, these models typically adopt a trade-off between the ability to investigate complex and realistic configurations and the prediction accuracy of the heat transfer associated with the phase change. This study developed a model to simulate a room with three-dimensional heat conduction in PCM-integrated walls and to analyze the surface heat balances with high resolution. The model was validated using experimental data of a passive solar test cell with a non-uniform and dynamic thermal environment. The model was then applied to investigate the PCMs integrated into the test cell during the summer. The PCM with

*Postal address: Bâtiment Sadi-Carnot, 9, rue de la Physique, Campus LyonTech La Doua, 69621 Villeurbanne cedex France

Email address: teddy.gresse@insa-lyon.fr (Teddy Gresse)

a narrow phase change temperature range and a thickness of approximately 10 mm was highly effective in reducing the indoor temperature fluctuations; the peak surface temperature was reduced by up to 6 °C in the sun patch, and the operative temperature fluctuations decreased by up to 2.6 °C. The PCM integration could be limited to the sun patch trajectory on the wall surfaces to optimize its utilization and limit the installation cost.

Keywords: Three-dimensional building energy modeling, Validation, Phase change material, Heat transfer, Latent heat storage.

Nomenclature

Latin letters

A	Area	[m ²]
C	Heat capacity	[J kg ⁻¹ K ⁻¹]
F	Form factor	[-]
h	Enthalpy	[J kg ⁻¹]
hc	Convective heat transfer coefficient	[W m ⁻² K ⁻¹]
Ir	Solar irradiance	[W m ⁻²]
K	Conductance	[W K ⁻¹]
M	Radiant exitance	[W m ⁻²]

R	Thermal resistivity	$[\text{m}^2 \text{K W}^{-1}]$
T	Temperature	$[\text{K or } ^\circ\text{C}]$

Grec letters

α	Absorptivity	$[-]$
β	Liquid fraction	$[-]$
Δt	Time step	$[\text{s}]$
δ	Cell size	$[\text{m}]$
γ	Angle of inclination of the walls from horizontal	$[\text{ }^\circ]$
λ	Thermal conductivity	$[\text{W m}^{-1} \text{K}^{-1}]$
μ	Expected value	$[-]$
ϕ	Heat flux	$[\text{W m}^{-2}]$
ρ	Density	$[\text{kg m}^{-3}]$
σ_{SD}	Standard deviation	$[-]$
ε	Emissivity	$[-]$

Subscripts

a	air
$glob$	global

<i>gnd</i>	ground
<i>i,j,k</i>	cell indices
<i>in</i>	inner
<i>loc</i>	local
<i>out</i>	outer
<i>sky</i>	sky
<i>x,y,z</i>	spatial directions
$E_{n/m}$	facet index

Superscripts

0	initial
<i>cond</i>	conductive
<i>conv</i>	convective
<i>dif</i>	diffuse
<i>dir</i>	direct
<i>eff</i>	effective
<i>LW</i>	long-wave
<i>new</i>	new

rad radiative

solid solidification

SW short-wave

tot total

Constants

σ_{SB} Stephan-Boltzmann constant $5.670 \times 10^{-8} \text{ W m}^{-2} \text{ K}^{-4}$

1. Introduction

The building sector accounts for one-third of global final energy consumption [1]. For several years, considerable efforts have been made in the field of building design to improve building energy efficiency. In particular, the incorporation of phase change materials (PCMs) into building envelopes has been investigated as a potential technology for enhancing building energy efficiency and indoor thermal comfort [2]. In contrast to traditional building materials, whose energy storage capabilities are restricted to sensible heat, the ability of PCMs to store energy is primarily characterized by their latent heat of fusion at small temperature intervals. PCMs can be used in building applications as separate building material components with encapsulation or stabilization, or integrated directly using the direct incorporation technique or impregnation [3].

14 Computational modeling of thermal energy storage is an effective tool for
15 evaluating the capabilities of PCMs to mitigate temperature fluctuations in
16 buildings. The latent heat evolution is generally accounted for in the gov-
17 erning equation using either the enthalpy [4, 5, 6] or heat capacity method
18 [7, 8, 9]. These methods require only one formulation of the heat equation for
19 the entire domain and avoid solving the melting front position in the PCM.
20 However, these simplified models generally ignore the hysteresis or subcool-
21 ing characteristics of some PCMs.

22 Various numerical models for simulating heat transfer in building enclosures
23 integrated with PCMs have been developed in the literature. Al-Saadi and
24 Zhai [10] and Lamrani et al. [11] reviewed the modeling methods generally
25 used for the PCMs in buildings. Most models assume one-dimensional (1D)
26 conduction. The simplest models considered only a single wall, such as that
27 of Kuznik et al. [12], who developed a numerical model for the single wall
28 with 1D heat transfer to investigate the energy storage of PCM wallboard. To
29 evaluate the energy accumulated in the wall, Kuznik et al. [12] employed an
30 inverse method based on the numerical modeling of the heat transfer in the
31 walls using the measured temperatures as the boundary conditions. Voelker
32 et al. [13] presented another simple model based on an energy balance to
33 characterize the mathematical process and estimate the temperature trend
34 in a PCM-equipped room. Some studies combined both approaches. For
35 example, Xu et al. [14] developed a model of multiple single walls with 1D
36 heat transfer considering convective and radiative heat fluxes. The indoor

37 air was modeled using heat balance to analyze the thermal performance of
38 the shape-stabilized PCM floor. Such models facilitate quick estimation of
39 the PCM's thermal performance with an approximation of the heat transfer
40 associated with the phase change.

41 Among the models based on the 1D heat equation, the comprehensive models
42 used prevalent building simulation programs such as ESP-r [15], EnergyPlus
43 [16], TRNSYS [17], or BuildSysPro [18]. For example, Heim and Clarke [19]
44 investigated the diurnal latent heat storage effect of a PCM-impregnated
45 gypsum plasterboard in a multi-zone, highly glazed and naturally ventilated
46 passive solar building with ESP-r. Evola et al. [20] performed simulations
47 of a typical European office building using EnergyPlus to investigate the
48 storage efficiency of the PCM wallboards and their effect on the thermal
49 comfort perceived by the occupants in the room. Stritih et al. [21] stud-
50 ied microencapsulated PCM walls using TRNSYS to reduce energy use in
51 a typical business office with variations in room temperature for different
52 percentages of microencapsulated PCM in walls. Kuznik et al. [22] modeled
53 the thermal behavior of a low-energy single-storey building using the simula-
54 tion environment Modelica with BuildSysPro library to evaluate the thermal
55 comfort inside the building. These models facilitate investigating more com-
56 plex and advanced design alternatives than the previously discussed simple
57 models. A network of thermal-based elements can be simulated considering
58 dynamic interactions between them.

59 However, a common limitation of all these modeling approaches is the 1D

60 heat transfer assumption. This is a source of substantial uncertainties, par-
61 ticularly while investigating thermal bridges, which cannot be modeled using
62 the 1D assumption. In addition, the 1D assumption implies that only one
63 surface temperature per wall is calculated, and the short-wave (SW) and
64 long-wave (LW) radiative fluxes are considered uniform on each wall, limit-
65 ing the detailed modeling of the indoor radiative environment.

66 Detailed studies solving the two-dimensional (2D) or three-dimensional (3D)
67 heat equations in walls typically used computational fluid dynamics (CFD)
68 commercial software ANSYS Fluent [23]. In particular, Diarce et al. [24]
69 used a 2D approach to model a ventilated active facade that includes a PCM
70 considering the LW radiative heat exchange between the different layers of
71 the facade. A mapped grid of 250,000 cells was generated over the geometry,
72 and a time step of 600 s was used, requiring several hours of computation
73 time on one core for the simulation of four complete days. Gowreesunker
74 and Tassou [25] conducted a validation study with a 3D approach to predict
75 the effect of PCM clay boards on the control of ventilated and non-ventilated
76 indoor environments without considering the radiation heat transfer. The 3D
77 room model comprised approximately 200,000 elements in the air and wall
78 domains and used a time step of 100 s. Several hours of computation on four
79 parallel cores simulated one phase change cycle. These detailed modeling ap-
80 proaches allow complex multiphysics problems to be solved. However, they
81 are rarely used for modeling PCMs primarily because of the implementa-
82 tion complexities and associated high computational costs. Moreover, these

83 modeling approaches limit the investigation to simulations of simple building
84 configurations and short durations.

85 Thus, various models exist to quantify the technical and economic feasi-
86 bility and the thermal control effectiveness of the PCMs in building applica-
87 tions. However, to reduce the computational intensity, these models consider
88 either complex building designs with simplistic heat transfer assumptions or
89 detailed CFD and heat transfer with simplistic building configurations, and
90 the simulated duration is short.

91 Hence, this study presents a model to investigate the 3D heat conduc-
92 tion in the room walls integrated with PCMs and to analyze the wall surface
93 heat balances with high resolution. In particular, the model is applied to the
94 study of PCMs integrated into a realistic building configuration, considering
95 the indoor solar gains that induce a non-uniform and dynamic thermal en-
96 vironment. To the best of the authors' knowledge, this is the first study of
97 this kind.

98 Section 2 introduces the general concepts of the developed model and pro-
99 vides the heat transfer and phase change governing equations, as well as the
100 inputs and outputs of the model. Section 3 presents the model validation us-
101 ing the BESTLab passive solar low-energy test cell of real size equipped with
102 a window [26]. Finally, Section 4 investigates and discusses the capability
103 and benefits of the implemented model for the optimization of the efficiency
104 and positioning of the PCMs integrated into the BESTLab test-cell walls in
105 the summer.

106 **2. Building modeling**

107 *2.1. General concepts*

108 Figure 1 schematizes the developed dynamic thermal model. The model
109 was designed to simulate a room with 3D heat conduction in the walls and to
110 analyze the surface heat balances with high resolution considering the con-
111 vective heat transfer and the LW and SW radiation heat transfer. The wall
112 discretization can be refined, and the model can handle a short computational
113 time step of approximately a second.

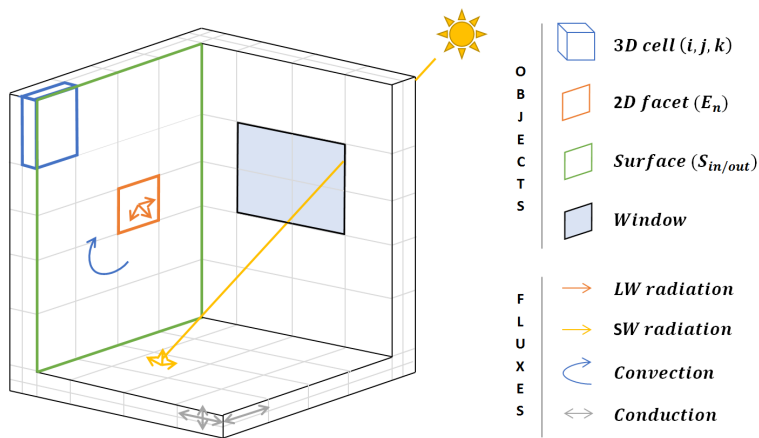


Figure 1: Schematic drawing of the 3D dynamic thermal model with heat fluxes.

114 The object-oriented paradigm is employed, allowing the definition of in-
115 teracting objects to accurately predict the thermal behavior of the room. In
116 particular, the model comprises the following four main objects.

- 117 • *3D Cell*: 3D element constituting the wall where the 3D heat equation
118 is solved using a finite-difference approach.

- 119 • *2D Facet*: 2D interface between the boundary of the *3D Cell* and its
120 direct thermal surrounding; the interface temperature is calculated by
121 solving the heat balance equation.
- 122 • *Surface*: inner or outer surface with its associated optical properties
123 (emissivity, absorptivity, and reflectivity) and boundary conditions. A
124 *Surface* comprises multiple *2D Facets*.
- 125 • *Window*: an opening that let the solar radiation enter the room creat-
126 ing a sun patch on the *Surfaces*.

127 Three boundary conditions are implemented in the model.

- 128 • Fixed temperature
- 129 • Fixed heat flux
- 130 • Dynamic heat flux, characterized by the following three thermal envi-
131 ronments.
 - 132 – *Room* (inner): nodal modeling of the air volume in free-running
133 mode, considering the convective and radiative fluxes over the
134 *2D Facets*.
 - 135 – *Adjacent Room* (outer): nodal modeling with a constant air tem-
136 perature, considering only convective flux over the *2D Facets*.
 - 137 – *Outdoors* (outer): weather data and solar position calculation,
138 considering convective and radiative fluxes over *2D Facets*.

139 Figure 2 presents the overall structure of the developed model. The basic
 140 equations are described in the following subsections.

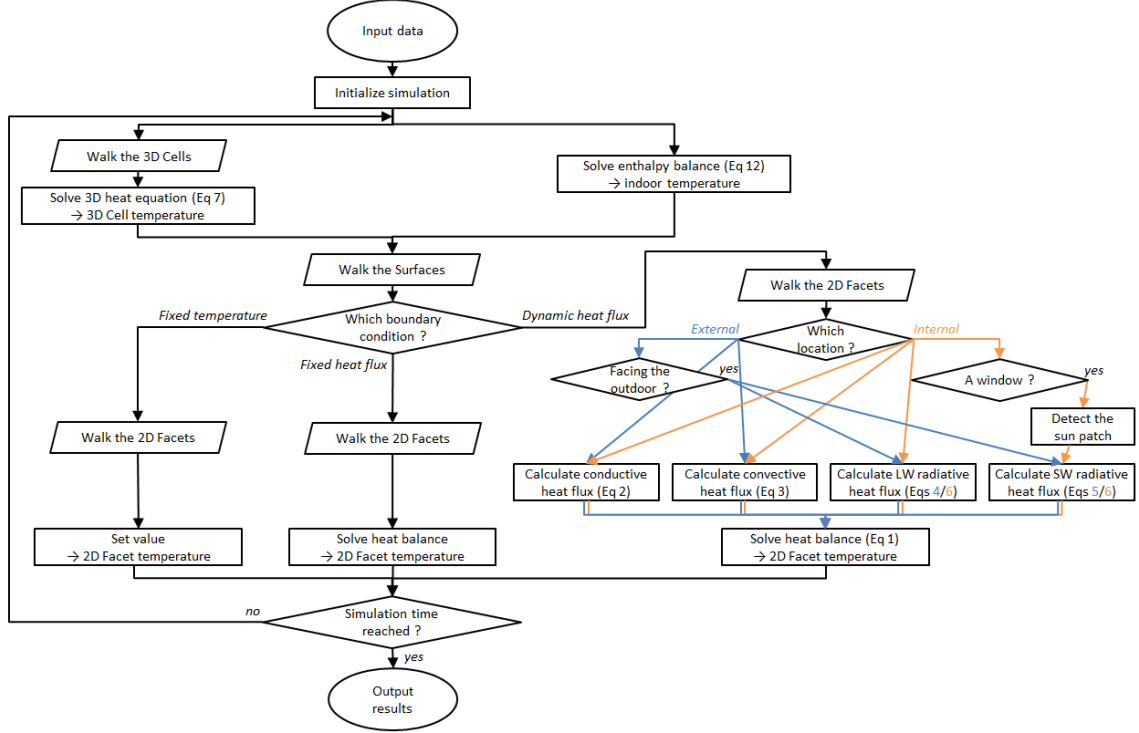


Figure 2: Flowchart for the model calculation procedure.

141 2.2. Surface heat balance

142 Consider boundary cell $(1, j, k)$ associated with facet E_n . If the convective
 143 and radiative (SW and LW) heat fluxes are considered, the heat balance is
 144 calculated over the facet as:

$$145 \quad \phi_{E_n}^{cond} + \phi_{E_n}^{conv} + \phi_{E_n}^{rad,LW} + \phi_{E_n}^{rad,SW} = 0 \quad (1)$$

146 Each term in Equation 1 is developed as follows.

147 *Conductive heat transfer.* Equation 2 gives the conductive heat flux $\phi_{E_n}^{cond}$
 148 $[\text{W m}^{-2}]$:

$$149 \quad \phi_{E_n}^{cond} = \frac{K_{1/2,j,k}}{A_{E_n}} \cdot (T_{1,j,k} - T_{E_n}), \quad (2)$$

150 where $K_{1/2,j,k} [\text{W K}^{-1}]$ is the conductance between cell $(1, j, k)$ and facet
 151 E_n , $A_{E_n} [\text{m}^2]$ is the facet area, $T_{1,j,k} [\text{K}]$ is the temperature of boundary cell
 152 $(1, j, k)$, and $T_{E_n} [\text{K}]$ is the temperature of facet E_n .

153 *Convective heat transfer.* Equation (3) gives the convective heat flux $\phi_{E_n}^{conv}$
 154 $[\text{W m}^{-2}]$ with the adjacent environment:

$$155 \quad \phi_{E_n}^{conv} = hc_{E_n} \cdot (T_a - T_{E_n}), \quad (3)$$

156 where $hc_{E_n} [\text{W m}^{-2} \text{K}^{-1}]$ denotes the convective heat transfer coefficient,
 157 and $T_a [\text{K}]$ denotes the air temperature of the adjacent environment.

158 *Radiative heat transfer.* The LW radiative flux on facet E_n that belongs to
 159 an external surface $\phi_{E_n,ex}^{rad,LW} [\text{W m}^{-2}]$ is calculated by a radiative balance with
 160 the ground at $T_{gnd} [\text{K}]$ and the sky at $T_{sky} [\text{K}]$:

$$161 \quad \phi_{E_n,ex}^{rad,LW} = \sigma_{SB} \cdot \varepsilon \cdot [F_{E_n,gnd} \cdot (T_{gnd}^4 - T_{E_n}^4) + F_{E_n,sky} \cdot (T_{sky}^4 - T_{E_n}^4)], \quad (4)$$

162 where $F_{E_n,gnd} = (1 - \cos(\gamma))/2$ and $F_{E_n,sky} = (1 + \cos(\gamma))/2$ are the form
 163 factors between facet E_n and the ground and between facet E_n and the sky,
 164 respectively, and γ is the angle of inclination of the walls from horizontal.

165 The SW radiative flux $\phi_{E_n,ex}^{rad,SW}$ [W m^{-2}] received by facet E_n on an exter-
 166 nal surface depends on the direct and diffuse solar irradiance:

$$167 \begin{cases} \phi_{E_n,ex}^{rad,SW} = \alpha_{E_n} \cdot (Ir_{E_n}^{dir,0} + Ir_{E_n}^{dif,0}) & \text{for facets facing the sun} \\ \phi_{E_n,ex}^{rad,SW} = \alpha_{E_n} \cdot Ir_{E_n}^{dif,0} & \text{for facets in the shadow} \end{cases} \quad (5)$$

168

169 If facet E_n is located on an internal surface, the radiative fluxes $\phi_{E_n,in}^{rad,LW}$ and
 170 $\phi_{E_n,in}^{rad,SW}$ [W m^{-2}] are calculated using the progressive refinement radiosity
 171 algorithm [27] based on the concept of shooting flux depicted in figure 3a.
 172 Solving the radiosity equation requires the form factors. In this model, the
 173 form factor calculation is based on the hemicube method, as illustrated in
 174 figure 3b. All the methodologies were adapted from Ashdown [28].

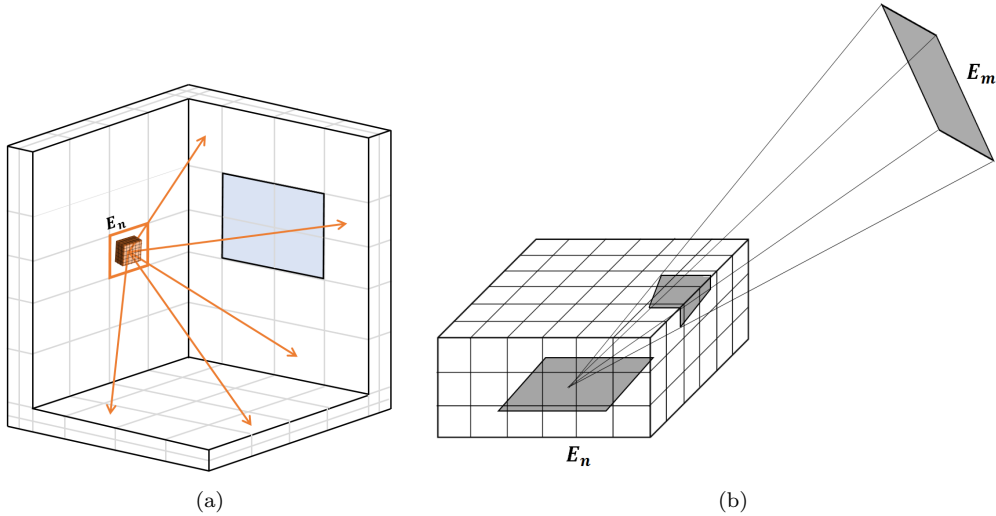


Figure 3: (a) Shooting flux process from facet E_n to the surrounding facets. (b) Form factor calculation between facets E_n and E_m using the hemicube method.

175 The radiosity approach shoots flux from one facet E_n to the surrounding
 176 facets that become secondary sources, shooting part of the flux that they
 177 receive to their surrounding facets. The process continues by always selecting
 178 the element that has the greatest amount of flux to shoot until the total
 179 amount of flux remaining in the environment is less than a predetermined
 180 fraction. This leads to a radiative balance over the interior facets, considering
 181 the multi-reflections. Equation 6 gives the net SW or LW radiative flux at
 182 facet E_n :

$$183 \quad \phi_{E_n, in}^{rad, SW/LW} = Ir_{E_n}^0 + \alpha_{E_n} \cdot \sum_{E_m} (M_{E_m} \cdot F_{E_n E_m}) - M_{E_n}^0, \quad (6)$$

184 where $Ir_{E_n}^0$ and $M_{E_n}^0$ [W m^{-2}] are the initial irradiance and radiant exitance
 185 of the facet, respectively, α_{E_n} is the SW absorptivity of the facet, M_{E_m}
 186 [W m^{-2}] is the radiant exitance of facet E_m (m represents the other facets),
 187 and $F_{E_n E_m}$ is the form factor from facets E_m to E_n .

188

189 For the LW contribution, the initial facet radiant exitance was calculated
 190 using the Stefan–Boltzmann law with no initial facet irradiance.

191 With respect to the SW contribution, the initial facet radiant exitance and
 192 irradiance are related to the sun patch detection using a geometric method.
 193 Figure 4 illustrates the detection, which consists of projecting the window
 194 frame and center of the interior facets onto a plan P perpendicular to the
 195 sunrays. No other buildings are considered outside. For facets detected

196 in the sun patch, the initial facet radiant exitance and irradiance are the
 197 reflected and absorbed fractions of the direct solar radiation transmitted
 198 by the window, respectively. For the interior facets of the window, a term
 199 corresponding to the transmitted diffuse solar radiation is considered.

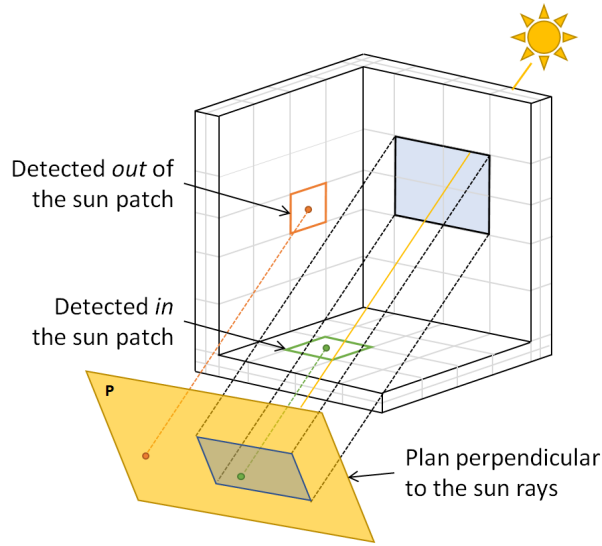


Figure 4: Sun patch detection process.

200 *Facet temperature calculation.* For a facet located on an external surface of
 201 a wall, the heat balance is solved using the TOMS 748 algorithm [29] to
 202 calculate T_{E_n} . This algorithm is a root-finding method without the use of
 203 derivatives from the C++ Boost library that is necessary as the LW radiative
 204 heat flux is non-linear (see equation 4).

205 For a facet located on an internal surface of a wall, the LW and SW radiative
 206 fluxes given in equation 6 are calculated with the facets temperature at the
 207 previous time step. This prevents the use of an iterative technique to calcu-

208 late the radiosity procedure that is time consuming. However, it may induces
 209 potential errors if the facets temperature evolution is significant between two
 210 iterations. Then, T_{E_n} is calculated from the heat balance.

211 2.3. Heat conduction inside walls

212 Within the walls, the thermal behavior of a cell (i, j, k) is governed by the
 213 3D heat equation solved using the forward Euler scheme for the time deriva-
 214 tive and central difference scheme for the second-order spatial derivatives:

$$\begin{aligned}
 & \rho_{i,j,k} \cdot C_{i,j,k} \cdot V_{i,j,k} \cdot \frac{T_{i,j,k}^{new} - T_{i,j,k}}{\Delta t} = \\
 & K_{i-1/2,j,k} \cdot (T_{i-1,j,k} - T_{i,j,k}) + \\
 & K_{i+1/2,j,k} \cdot (T_{i+1,j,k} - T_{i,j,k}) + \\
 215 & K_{i,j-1/2,k} \cdot (T_{i,j-1,k} - T_{i,j,k}) + \tag{7} \\
 & K_{i,j+1/2,k} \cdot (T_{i,j+1,k} - T_{i,j,k}) + \\
 & K_{i,j,k-1/2} \cdot (T_{i,j,k-1} - T_{i,j,k}) + \\
 & K_{i,j,k+1/2} \cdot (T_{i,j,k+1} - T_{i,j,k}),
 \end{aligned}$$

216 where ρ [kg m^{-3}] is the wall material density, C [$\text{J kg}^{-1} \text{K}^{-1}$] is the wall
 217 material heat capacity, V [m^3] is the cell volume, K [W K^{-1}] is the conduc-
 218 tance at the interface between the cell and adjacent cells, and T [K] is the
 219 cell temperature.

220 The conductance $K_{i+1/2,j,k}$ between two cells (i, j, k) and $(i + 1, j, k)$ is cal-

221 culated as follows:

$$222 \quad K_{i+1/2,j,k} = \frac{\delta y_j \cdot \delta z_k}{\delta x_i/2\lambda_{i,j,k} + \delta x_{i+1}/2\lambda_{i+1,j,k} + R_{i+1/2,j,k}}, \quad (8)$$

223 where $\lambda_{i,j,k}$ and $\lambda_{i+1,j,k}$ [$\text{W m}^{-1} \text{K}^{-1}$] are the thermal conductivities of
 224 cells (i, j, k) and $(i + 1, j, k)$, respectively, $R_{i+1/2,j,k}$ [$\text{m}^2 \text{K W}^{-1}$] is the thermal
 225 resistivity of the interface between these two cells, and δx_i , δy_j , and δz_k [m]
 226 are the cell dimensions in the x , y , and z directions, respectively.

227 The explicit formulation of the 3D heat equation imposes a stability cri-
 228 terion that must be satisfied for all the cells (i, j, k) . The smallest stable time
 229 step is used for all the cells to guarantee stability.

230 2.4. Heat conduction inside PCM

231 The PCM is modeled using an effective capacity method. In this method,
 232 the heat capacity is treated as a function of temperature in the phase change
 233 temperature range. The effective heat capacity increases and decreases sharply
 234 with an apparent peak when the PCM melts or solidifies during energy stor-
 235 age or latent heat release, respectively. The present model assumes that the
 236 effective heat capacity of a cell (i, j, k) varies as a Gaussian function as:

$$237 \quad C_{i,j,k}^{eff}(T_{i,j,k}) = C_{i,j,k}^{eff,solid} + \frac{h^{tot}}{\sigma_{SD}\sqrt{2\pi}} e^{-\frac{(T_{i,j,k}-\mu)^2}{2\sigma_{SD}^2}}, \quad (9)$$

238 where $C_{i,j,k}^{eff,solid}$ [$\text{J kg}^{-1} \text{K}^{-1}$] is the effective heat capacity of the PCM in the
 239 solid phase when the PCM is fully discharged, h^{tot} [J kg^{-1}] is the enthalpy

240 of a complete phase change of the PCM, σ_{SD} is the standard deviation, and
 241 μ is the expected value. The same heat capacity is considered for the PCM
 242 in the solid and liquid phases. The density and thermal conductivity of the
 243 PCM are constant.

244 The local liquid fraction β_{loc} of a cell (i, j, k) , given by Equation 10, is
 245 the ratio of the enthalpy of the PCM at a given temperature ($h(T_{i,j,k})$) to
 246 the total enthalpy of the PCM (h^{tot}). $h(T_{i,j,k})$ is calculated as the integral of
 247 the effective heat capacity between T^{solid} , which is the temperature at which
 248 complete solidification is achieved, and $T_{i,j,k}$, which is the temperature of the
 249 cell. h^{tot} is a known parameter in the Gaussian function. In the solid phase,
 250 $\beta_{loc} = 0$; in the liquid phase, $\beta_{loc} = 1$; β_{loc} varies between 0 and 1 during the
 251 phase change.

$$252 \quad \beta_{loc} = \frac{h(T_{i,j,k})}{h^{tot}}, \quad h(T_{i,j,k}) = \int_{T^{solid}}^{T_{i,j,k}} C_{PCM} dT \quad (10)$$

253 A global liquid fraction β_{glob} represents the overall state of the PCM,
 254 given by:

$$255 \quad \beta_{glob} = \frac{\sum h(T_{i,j,k}) \cdot m_{i,j,k}}{h^{tot} \cdot m^{tot}}, \quad (11)$$

256 where $m_{i,j,k}$ is the mass of each cell that comprises the PCM, and m^{tot} is
 257 the total mass of the PCM.

258 2.5. Room

259 The indoor environment is modeled as a single node, and the air temper-
 260 ature $T_{a,in}$ [K] is calculated by an enthalpy balance using the forward Euler

261 scheme for the time derivative as:

$$\begin{aligned}
 & \rho_{a,in} \cdot C_{a,in} \cdot V_r \cdot \frac{T_{a,in}^{new} - T_{a,in}}{\Delta t} = \\
 262 \quad & \sum_N (\dot{m}_N \cdot C_{a,in} \cdot (T_{a,N} - T_{a,in})) + \sum_{E_m} (A_{E_m} \cdot hc_{E_m} \cdot (T_{E_m} - T_{a,in})), \quad (12)
 \end{aligned}$$

263 where $\rho_{a,in}$ [kg m^{-3}] is the air density, $C_{a,in}$ [$\text{J kg}^{-1} \text{K}^{-1}$] is the heat ca-
 264 pacity of the air, V_r [m^3] is the volume of the room, N is the number of
 265 external zones that can be adjacent rooms or the outdoors, \dot{m}_N [kg s^{-1}] is
 266 the air leakage rate for the corresponding zone, $T_{a,N}$ [K] is the dry bulb tem-
 267 perature of the corresponding zone, and A_{E_m} [m^2], hc_{E_m} , and T_{E_m} [K] are
 268 the area, convective heat transfer coefficient, and temperature of facet E_m ,
 269 respectively. It is reminded that the LW and SW radiative heat fluxes are
 270 taken it account in T_{E_m} calculation as detailed in subsection 2.2.

271 2.6. Input and output of the model

272 The model is developed in C++ and compiled with the G++ compiler.
 273 To run a simulation using the model, several input data must be specified:

- 274 • The building geometry, wall composition (heat capacity and thermal
 275 conductivity), and mesh are generated using the HEAT3 [30] software.
 276 This software includes a 3D mesh generator and building material li-
 277 brary.
- 278 • The boundary conditions (flux or temperature) and the boundary ther-
 279 mal environments (adjacent rooms or the outdoors). Weather data

280 must be provided when the outdoor environment is considered.

- 281 • The wall surface and air physical properties.
- 282 • The initial conditions (new or from a previous simulation).
- 283 • General information on the building (location coordinates and building
284 orientation).
- 285 • If the PCM is modeled, the different parameters to define the Gaussian
286 function of the effective heat capacity.

287 This model provides different types of output data:

- 288 • The temperature field on the walls in the Hierarchical Data Format
289 (HDF5),
- 290 • The heat fluxes and temperature fields on the surfaces in Hierarchical
291 Data Format (HDF5),
- 292 • The indoor air temperature in the text format,
- 293 • The temperatures at specific surface locations in the text format,
- 294 • The global heat flux over the interior surfaces in the text format,
- 295 • The local and global liquid fractions of the PCM in the text format.

296 An XMF file is generated along with the HDF5 file read the output fields
297 with an appropriate application such as Paraview.

298 **3. Validation of the model without PCM**

299 *3.1. Experimental reference*

300 The experimental reference is the BESTLab full-scale low-energy test cell
301 [31] developed in EDF R&D laboratory and investigated by Rodler [26]. The
302 facility is located approximately 75 km southeast of Paris (latitude: 48°22' N;
303 longitude: 2°49' E; altitude: 100 m) in a rural environment without obstacles
304 on the south and west sides for a distance of 100 m.

305 The test cell is a room with dimensions of $2.97 \times 2.89 \times 2.82$ m³ and is
306 illustrated in figure 5. The west wall faces the outdoors and is equipped with
307 a double-glazed window. The three other walls, namely the east, south, and
308 north walls, are surrounded by a thermal guard well-controlled by heating/air-
309 conditioning systems at a constant temperature. A thermally insulated closed
310 door on the east wall provides access to the thermal guard.

311 Figure 6a shows the wall composition. The east, south, and north walls
312 are 41 cm thick, and the west wall is 32.4 cm thick. The thermal character-
313 istics of the materials and the characteristics of the window are provided in
314 Tables 1 and 2.

315 Ten PT100 probes were installed at different locations on the interior wall
316 surfaces to measure the temperature. The validation focuses on one probe
317 on each wall, namely probes *PW*, *PE*, *PN*, *PS*, *PF*, and *PC*, as illustrated
318 in figure 5. The indoor air temperature was measured with three radiation-
319 shielded PT100 probes, *PA1*, *PA2*, and *PA3*, located in the middle of the
320 room at the bottom, center, and top regions of the air volume, respectively, to

321 consider the potential heterogeneity of the temperature due to stratification.
 322 The temperature at $PA2$, also referred to as PA , is used for the validation.

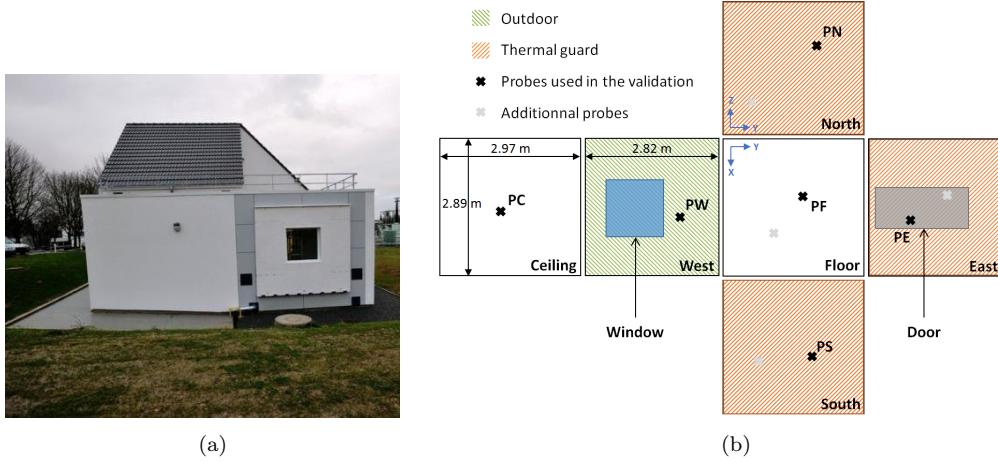


Figure 5: (a) Photograph of the west test cell [26]. (b) Developed view of the west test cell illustrating the different probe locations and boundary environments.

Table 1: Materials and thermal characteristics of the layers constituting the walls.

Material	λ [$\text{W m}^{-1} \text{K}^{-1}$]	ρ [kg m^{-3}]	C [$\text{J kg}^{-1} \text{K}^{-1}$]
Blocks	0.8	800	1000
Coat	0.5	1300	1000
Concrete	1.75	2500	1000
Drywall	0.313	816	800
EPS insulation	0.032	14	1400
XPS insulation	0.029	33	1400
Fermacell	0.32	1150	1265
Mineral wool	0.04	33	1400
Wood	0.120	1250	1200

323 The period used for the validation was a week from the 8th of May 2013
 324 to the 16th of May 2013. During this period, the average outdoor air tem-
 325 perature was 13°C , with a maximum during the daytime at 18.7°C and a

Table 2: Optical and thermal characteristics of the window.

Transmissivity	Reflectivity	Absorptivity	Heat transfer coefficient [W m ⁻² K ⁻¹]
0.52	0.28	0.18	1.12

326 minimum during the nighttime at 5.6 °C, and the maximum horizontal global
 327 solar radiation varied from 400 to 800 W m⁻².

328 3.2. Model settings

329 The exterior boundary conditions are either fluxes or temperatures. For
 330 the west wall that faces the outdoors, dynamic convective and radiative fluxes
 331 were applied. Minute-wise weather data were used from meteorological sta-
 332 tion "Les Renardières" of the EDF Lab site. The air temperature, solar
 333 radiation, and wind conditions were obtained from the measurements per-
 334 formed in the direct vicinity of the test cell. Table 3 details the instruments
 335 and accuracies of the sensors used by the meteorological station. For the
 336 east, north, and south walls, that are surrounded by a thermal guard, only
 337 a dynamic convective flux was considered. The thermal guard was modeled
 338 as a constant air temperature node at 20 °C. On the floor and the roof a
 339 constant temperature of 19 °C was set according to Rodler [26].

340 The room was operating in free-running mode and the model accounted for
 341 the convective contribution between the room air node and the interior wall
 342 surfaces, the LW radiative contribution between the interior wall surfaces
 343 and the SW radiative contribution with the sun patch detection and multi-
 344 reflections.

345 The natural convection was modeled with the empirical correlations from
 346 McAdams [32] for outdoor conditions and Awbi and Hatton [33] for indoor
 347 conditions, i.e., at the interior surfaces and the exterior surfaces adjacent to
 348 the thermal guard.

Table 3: Equipment of the meteorological station "Les Renardières".

Measurement	Instrument	Accuracy
Air temperature	PT100 probe	$\pm 0.2^\circ\text{C}$
Wind velocity	CAF2 anemometer (Chauvin Arnoux)	$\pm 1\%$
Global horizontal solar radiation	CM21 pyranometer (Kipp & Zonen)	$\pm 0.2\%$
Diffuse horizontal solar radiation	CM11 pyranometer (Kipp & Zonen)	$\pm 0.6\%$

349 Previously, numerical studies were conducted by Rodler [26] to assess the
 350 importance of weather data sampling and to analyze and optimize the mesh
 351 size for this room. Figures 6a and 6b show the resulting discretization for
 352 the wall volumes and interior wall surfaces, respectively. The total num-
 353 ber of cells, exterior facets, and interior facets was 22780, 5300, and 560,
 354 respectively.

355 Three days of initial simulations removed the influence of the initial con-
 356 ditions while accounting for the real environmental history. A constant time
 357 step of 4.08 s was used. The computational time was approximately 8.4 h
 358 over one processor (Intel(R) Xeon(R) Gold 5120 CPU @ 2.20GHz) for simu-
 359 lating eight days. The results were averaged over each minute for comparison
 360 with the experimental results.

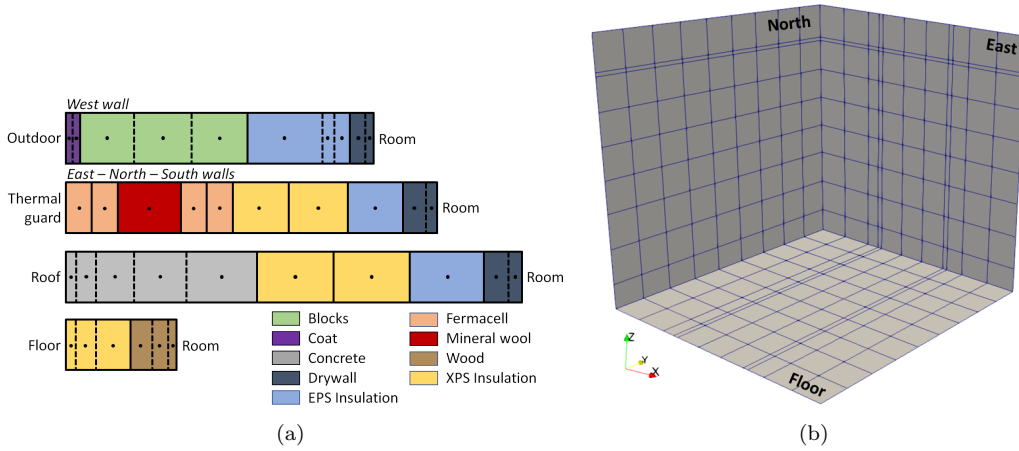


Figure 6: (a) Wall composition and discretization. (b) Interior-surface discretization.

361 *3.3. Results and discussion*

362 Figure 7a shows the surface and air temperatures at the different probe
 363 locations. At the surface probes located on the sun trajectory, namely PF ,
 364 PE , and PS , the temperature peaked up to $43\text{ }^{\circ}\text{C}$ during the daytime because
 365 of the direct SW solar radiation. The temperature evolution is similar at the
 366 surface probes outside of the sun trajectory (namely PW , PC , and PN) and
 367 air probe (PA), and the temperature varies from $20\text{ }^{\circ}\text{C}$ during the nighttime
 368 to $28.5\text{ }^{\circ}\text{C}$ during the daytime. As the test cell is thermally well-insulated,
 369 the temperature decrease during nighttime is limited, leading to relatively
 370 high average indoor surface and air temperatures of approximately $24\text{ }^{\circ}\text{C}$.

371 Figures 7b and 7c show the simulated and measured temperatures at PE
 372 and PA on the 11th of May 2013 from 4:00 p.m. to 11:59 p.m. The sun
 373 patch is detected earlier by the model at PE . This is partly because of the
 374 surface mesh discretization implying that the surface probes are considered

375 2D facets, rather than points (as it is experimentally). The temperature
376 peak is also overestimated, and the temperature variations when the probe
377 is located on the sun trajectory do not always match the measurements.
378 This might be due to errors in the weather data file or heat flux estimation,
379 leading to inaccurate heat balance calculation. It could also be due to using
380 an explicit method for the solution of the governing equations. In addition,
381 the air temperature is overpredicted when the sun patch is inside the room.
382 This can be attributed to the surface temperature overprediction in the sun
383 patch, as observed at *PE*.

384 Figure 8 shows the statistics in boxplots of the deviation between the sim-
385 ulated and measured temperatures over the study period. The median tem-
386 perature deviation is less than 0.2°C with an interquartile range varying from
387 0.5°C to 0.7°C . The maximum temperature deviations do not exceed 2°C
388 for the probes outside the sun trajectory but are significantly higher for the
389 probes receiving solar radiation, reaching up to 10°C at *PE*. The marginal
390 median temperature deviation between the measurements and simulations
391 for all probes confirms that no bias is introduced in the simulation results.
392 The significant difference between the interquartile ranges and the maximum
393 temperature deviations at *PE* and *PF* is the sign of abrupt changes in ther-
394 mal loads induced by the sun patch that may not be simultaneous in the
395 model and reality.

396 Table 4 lists the errors in the daily maximum temperature ($\Delta T|_{max}$), as
397 well as the root mean square errors (*RMSE*) at the different probe loca-

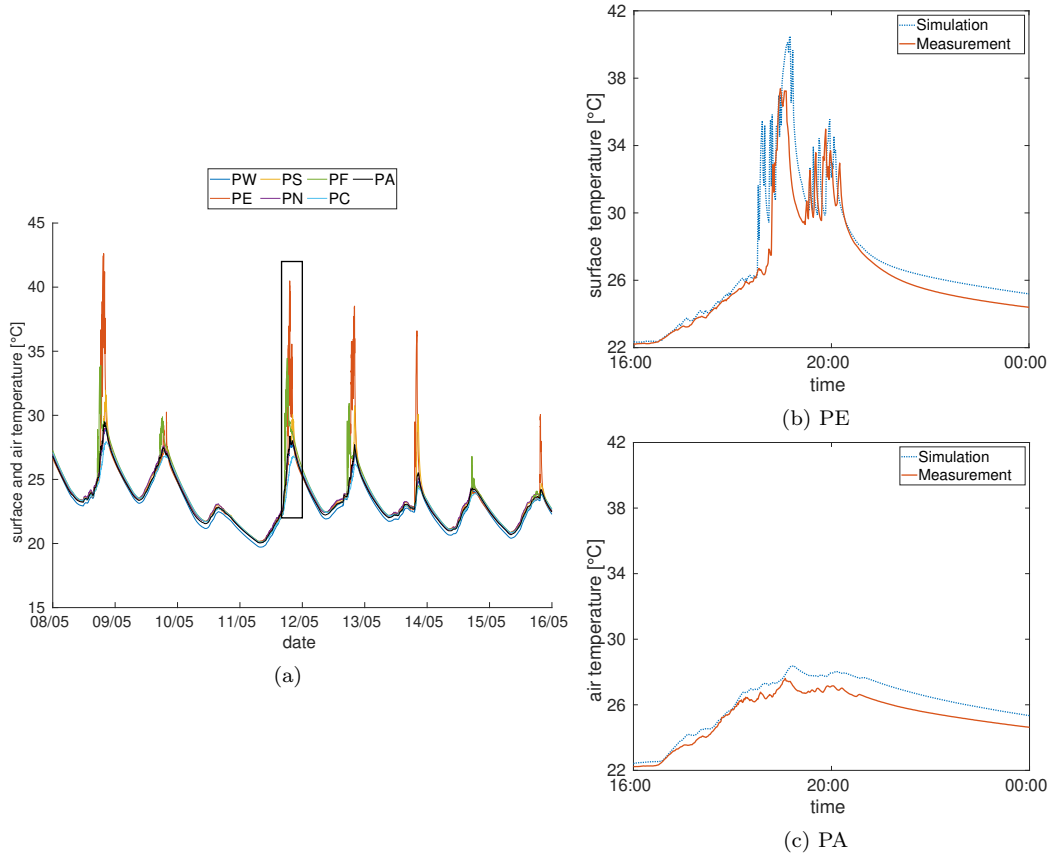


Figure 7: (a) Simulated surface temperatures over the studied period at the different probe locations. The black box indicates the period used for the comparison with the experiment. (b)–(c) Comparison of measured and simulated surface temperatures at *PE* and *PA* on the 11th of May 2013.

398 tions. Probes *PE*, *PS*, and *PF*, which receive direct solar radiation, have
 399 the highest $\Delta T|_{max}$ values, varying between 3 °C and 4 °C; the $\Delta T|_{max}$ val-
 400 ues for probes *PW*, *PN*, and *PC* outside the sun trajectory and *PA* are
 401 below 1.6 °C. Further interpretations are not possible because of the lack of
 402 propagation errors, which can be significant for high solar gains, in the ex-
 403 perimental acquisition chain. However, the $\Delta T|_{max}$ values are well below the

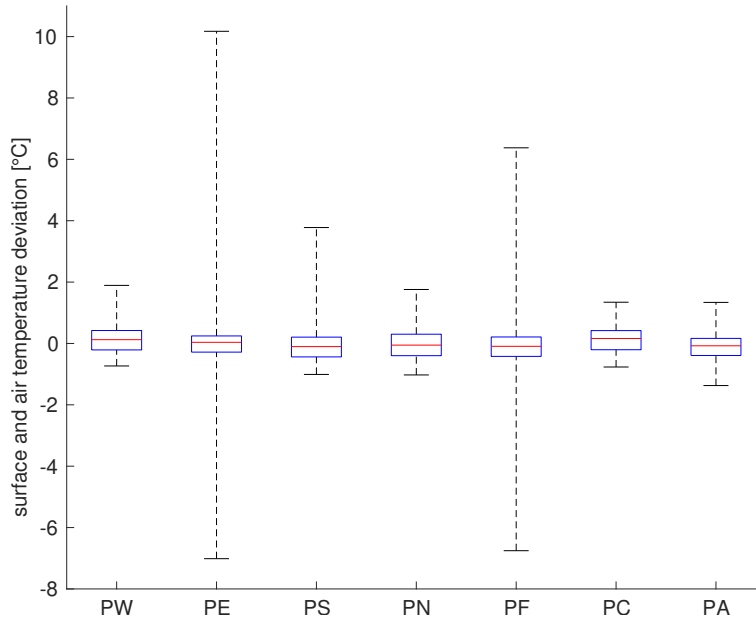


Figure 8: Boxplots at the different probe locations. The red central mark indicates the median, and the bottom and top edges of the box indicate the 25th and 75th percentiles, respectively. The whiskers extend to the most extreme data points.

404 significant difference between the interquartile ranges and the maximum tem-
 405 perature deviations at *PE* and *PF* presented above, confirming that these
 406 deviations can be attributed to a one-time delay in the sun patch detection
 407 and do not significantly deteriorate the overall temperature prediction. As
 408 for the $\Delta T|_{max}$ values, the *RMSE* values are higher for probes *PE* and *PF*
 409 that received direct solar radiation, but the values did not exceed 0.75°C
 410 for all probes. This confirms the close agreement between the measurements
 411 and simulations.

Table 4: Errors in daily maximum temperature and RMSE for surface and air at the different probe locations.

Probe	PW	PE	PS	PN	PF	PC	PA
$\Delta T _{max}$ [°C]	1.56	3.10	3.32	1.54	3.89	1.32	0.77
RMSE [°C]	0.47	0.74	0.53	0.50	0.73	0.43	0.42

412 4. Application to PCM integrated into walls

413 The model was applied to study PCMs in the BESTLab test cell, the ex-
414 perimental reference used for the validation, in the summer from 12:00 a.m.
415 on the 13th of July 2013 to 12:00 a.m. on the 16th of July 2013. During
416 this period, the average outdoor air temperature was 21.8°C with a maxi-
417 mum during the daytime at 30.8°C and a minimum during the nighttime at
418 12.6°C . The maximum horizontal global solar radiation was approximately
419 900 W m^{-2} .

420 4.1. Model settings

421 Figure 9 shows the heat capacities of the two selected PCMs, namely
422 *PCM1* and *PCM2*, derived from the PCM studied by Kuznik et al. [34]
423 which is constituted of 60% of micro-encapsulated PCM and developed by
424 the DuPont de Nemours compagny. The peak melting temperature was set
425 at 35°C corresponding to the mean surface temperature of the walls receiving
426 solar radiation. Also, the width of the phase change temperature range T_{pc}
427 was adjusted with a large one for *PCM1* and a narrow one for *PCM2*. As
428 the total enthalpy is kept the same, the Gaussian function for the effective
429 heat capacity of *PCM2* increases and decreases more sharply than that of
430 *PCM1*. The natural convection is modeled with the empirical correlation
431 from Awbi and Hatton [33] as for the validation without PCM. The thermal
432 characteristics of the reference and the two PCMs studied are given in Ta-
433 ble 5.

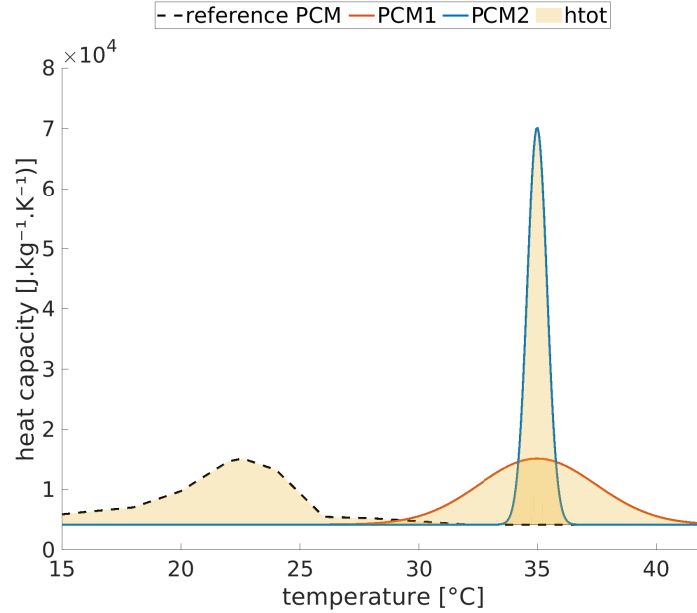


Figure 9: Heat capacities of the reference PCM and the two PCMs studied. The total enthalpy is represented by yellow areas.

Table 5: Thermal characteristics of the reference PCM and the two PCMs studied.

Properties		reference [34]	<i>PCM1</i>	<i>PCM2</i>
ρ	$[\text{kg m}^{-3}]$	1019	1019	1019
λ	$[\text{W m}^{-1} \text{K}^{-1}]$	0.2	0.2	0.2
h_{tot}	$[\text{J kg}^{-1}]$	67800	67800	678000
T_{pc}	$[\text{°C}]$	[18,26]	[28,42]	[34,36]
$C_{peak/solid}$	$[\text{J kg}^{-1} \text{K}^{-1}]$	15150/4200	15150/4200	70000/4200
hc	$[\text{W m}^{-2} \text{K}^{-1}]$	–	Awbi and Hatton correlation [33]	

435 Figure 10 illustrates the PCM configurations investigated and their posi-
 436 tions in the test cell. The three configurations studied are:

- 437 • *C0*: base case (no PCM).

- 438 • $C1$: $C0$ + 22 mm PCM panel on the floor.
- 439 • $C2$: $C0$ + 7.6 mm PCM panel on each wall facing the window (the
- 440 north, south, and east walls).

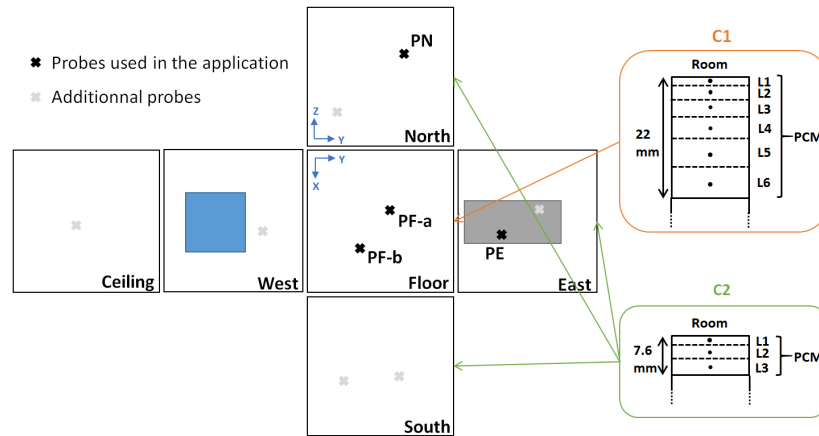


Figure 10: Developed view of the west test cell illustrating the different probe locations and studied PCM configurations $C1$ and $C2$. The PCM's discretization is illustrated by dotted lines.

441 The volumes of the PCM embedded in $C1$ and $C2$ were equivalent. The

442 PCMs were integrated as panels covering the entire wall or floor surface and

443 substituted the first wall material layer, which was the parquet in $C1$ and the

444 drywall in $C2$. In $C0$, a material with the same density and conductivity as

445 the studied PCM was integrated at the PCM locations in $C1$ and $C2$, with

446 a constant heat capacity equal to the heat capacity of the PCM in the solid

447 phase. This adaptation in $C0$ allowed the evaluation of the specific impact

448 of the latent heat storage of the PCMs on the temperature evolution in the

449 ROOM.

450

451 The same boundary conditions as in the validation were applied with
452 the adapted data: the outdoors was modeled with minute-wise weather data
453 of the studied period, constant air temperature node modeling the thermal
454 guard was maintained at 20 °C, and floor and the roof exterior surface tem-
455 perature was set at 20.5 °C.

456 In the three configurations, the same mesh as in the validation was used ex-
457 cept at the PCM's locations where the mesh was refined. A grid sensitivity
458 analysis of the PCM discretization in the direction perpendicular to the wall
459 surface was performed. Three meshes were tested as follows:

- 460 • three layers on the floor and one layer on the walls,
- 461 • six layers on the floor and two layers on the walls,
- 462 • twelve layers on the floor and four layers on the walls.

463 The maximum surface temperature deviation between the grids appeared
464 during the daytime in the sun patch with a deviation of approximately 1 °C.
465 The refinement of the first layer appears to be the most influential param-
466 eter. Thus, the selected mesh was refined using six layers ($L1-L6$) on the
467 floor and three layers ($L1-L3$) on the walls with progressive refinement to
468 get a thin first layers near the wall surface, as illustrated in figure 10.

469 Three days of initial simulations removed the influence of the initial condi-
470 tions while accounting for the real environmental history. A constant time
471 step of 0.71 s was used. The computational time was approximately 22.4 h

472 over one processor (Intel(R) Xeon(R) Gold 5120 CPU @ 2.20GHz) for sim-
473 ulating three days. The two probes on the floor ($PF - a$ and $PF - b$) and
474 one probe on each of the walls facing the window (PN , PE , and PS) were
475 monitored.

476

477 4.2. Results

478 4.2.1. Global liquid fractions

479 Figure 11 plots $PCM1$ and $PCM2$ global liquid fractions $\beta_{glob,PCM1}$ and
480 $\beta_{glob,PCM2}$ in $C1$ and $C2$. $\beta_{glob,PCM1}$ varies from 0.05 to 0.36 in $C1$ and 0 to
481 0.42 in $C2$. The variation in $\beta_{glob,PCM2}$ is significant, ranging from 0.23 to
482 0.5 in $C1$ and 0.2 to 0.58 in $C2$. Since the phase change is more dominant
483 with $PCM1$ than with $PCM2$, the global latent heat storage is improved
484 using $PCM1$ during the study period. Moreover, $\beta_{glob,PCM1}$ and $\beta_{glob,PCM2}$
485 variations are similar in $C1$ and in each PCM panels in $C2$ while the PCM is
486 thicker in $C1$ than in $C2$. This could be due to a phase change predominant
487 in the superficial layers of the PCM. As the phase change is simultaneous in
488 the three PCM panels in $C2$ with its surface area approximately three times
489 that of $C1$, the PCM utilization in $C2$ is enhanced.

490 4.2.2. Local liquid fractions

491 *Distribution throughout layers.* Figures 12 and 13 plot $PCM1$ and $PCM2$
492 local liquid fractions $\beta_{loc,PCM1}$ and $\beta_{loc,PCM2}$ at the probes in $C1$ and $C2$,
493 respectively. At $PF - a$ located in the sun patch in $C1$, the peak of $\beta_{loc,PCM1}$

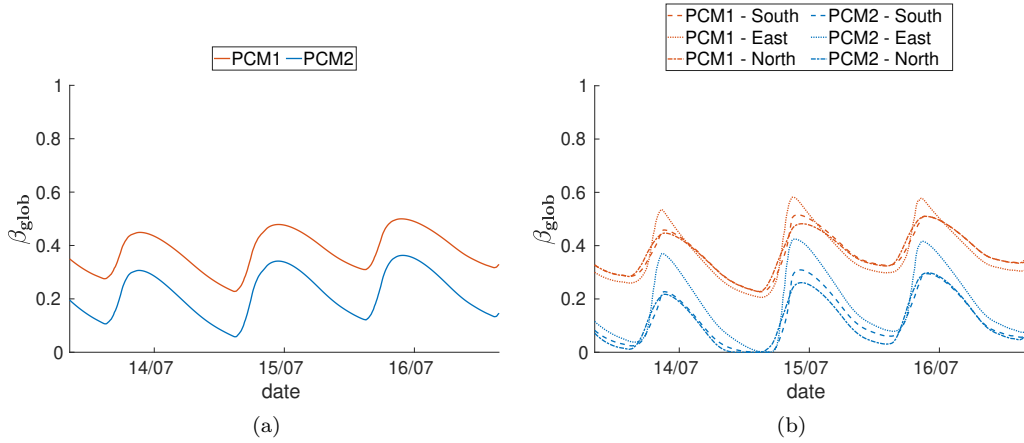


Figure 11: (a) Global liquid fraction in $C1$. (b) Global liquid fraction in $C2$.

494 and $\beta_{loc,PCM2}$ decrease from 0.98 to 0.66 and 1 to 0.58, respectively, from
 495 $L1$ to $L6$. However, the observation is different at PE located in the sun
 496 patch in $C2$, where $\beta_{loc,PCM1}$ and $\beta_{loc,PCM2}$ are almost always above 0.9 from
 497 $L1$ to $L3$. This confirms that a major part of the latent heat is stored in a
 498 thin superficial layer, and the storage decreases with depth inside the PCM.
 499 The time required for the heat to penetrate the PCM is larger than 12 h for
 500 layers $L5$ and $L6$ in $C1$, and the storage process cannot be completed in a
 501 day. Moreover, the extent of phase change is larger in $PCM2$ than in $PCM1$
 502 in areas that receive solar radiation. In fact, $\beta_{loc,PCM2}$ variations are larger
 503 than those of $\beta_{loc,PCM1}$ at the probes located in the sun patch, namely $PF-a$
 504 in $C1$ and PE in $C2$. However, outside the sun trajectory, as observed at
 505 probes $PF-b$ in $C1$ and PN in $C2$, $\beta_{loc,PCM2}$ is predominantly below 0.2.
 506 With $PCM1$, there is a phase change, but it is partial, without complete
 507 melting.

508 *Distribution over surfaces.* Figures 14 and 15 depict the distributions of
 509 $\beta_{loc,PCM2}$ in the superficial layer and the SW heat flux on the floor in *C1*
 510 and east wall in *C2*, respectively. The distributions averaged over the whole
 511 day of the 14th of July 2013 are presented. The results show significant het-
 512 erogeneities in $\beta_{loc,PCM2}$ distribution and the SW heat flux field. The phase
 513 change is dominant only where the SW heat flux is strong. Thus, the PCMs
 514 store latent heat when exposed to the sun patch with negligible storage in
 515 areas outside the sun trajectory.

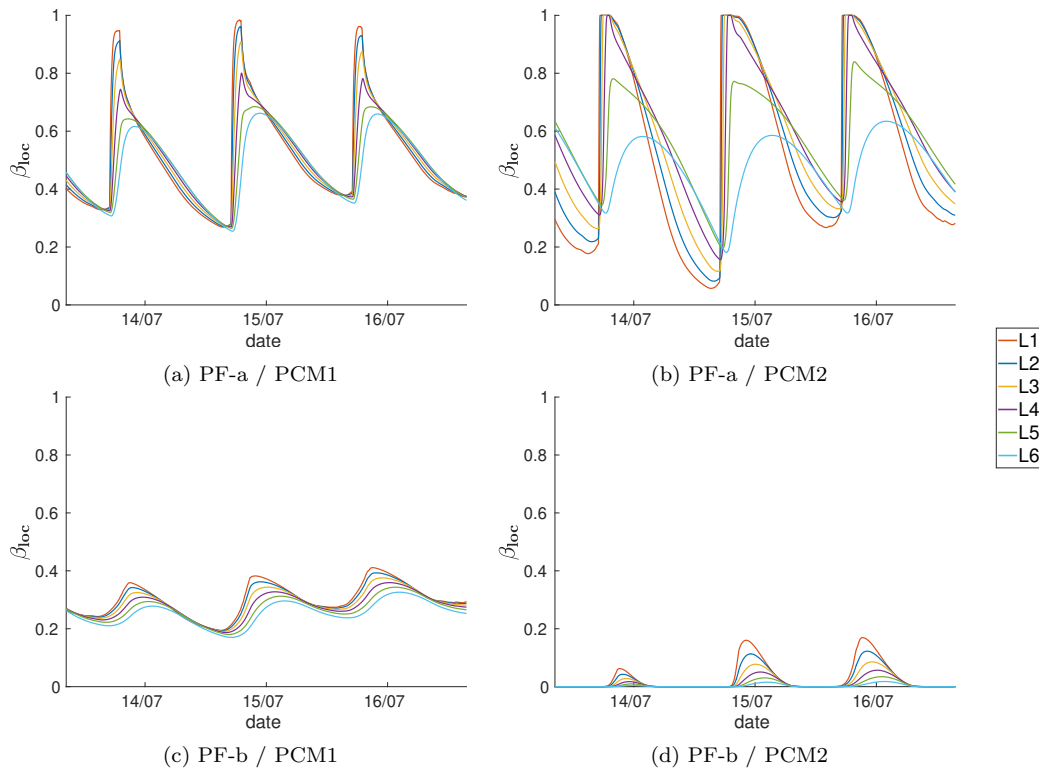


Figure 12: Local liquid fractions in *C1*.

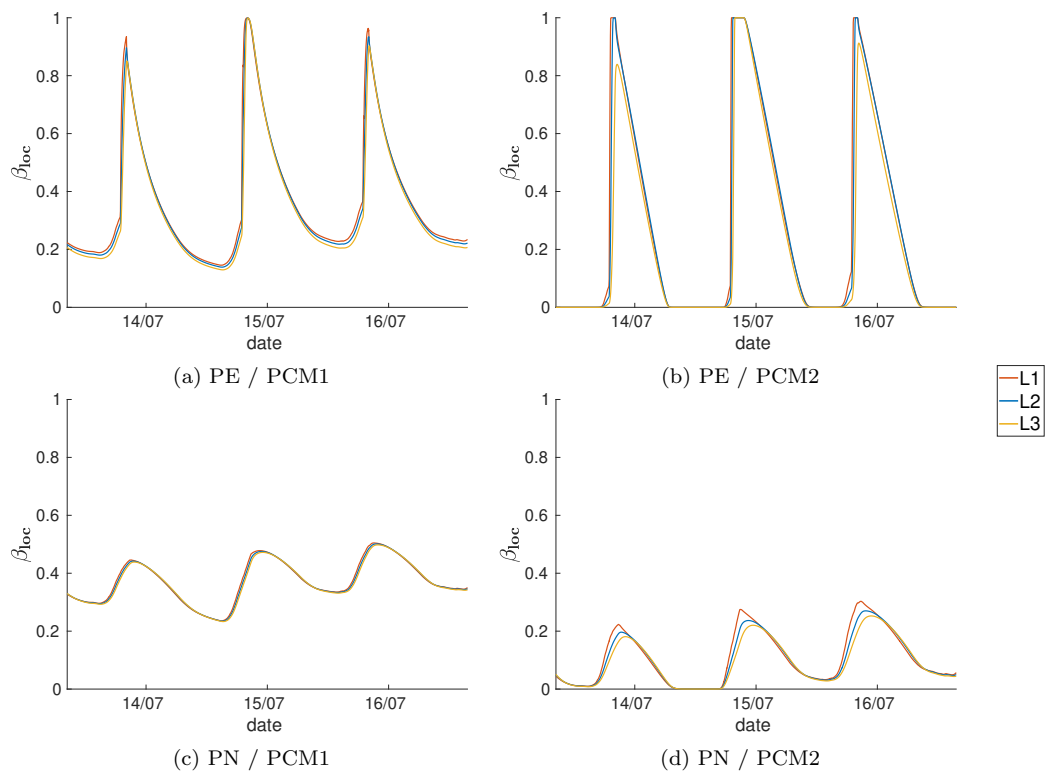


Figure 13: Local liquid fractions in $C2$.

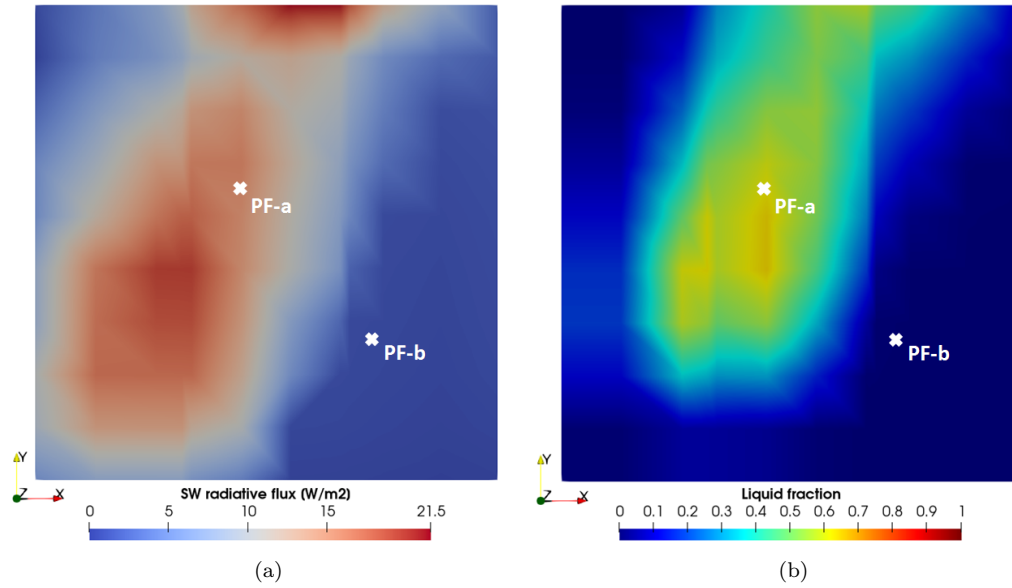


Figure 14: (a) Average SW heat flux distribution and (b) average liquid fraction distribution on the floor in the superficial layer of *PCM2* in *C1* the 14th of July 2013.

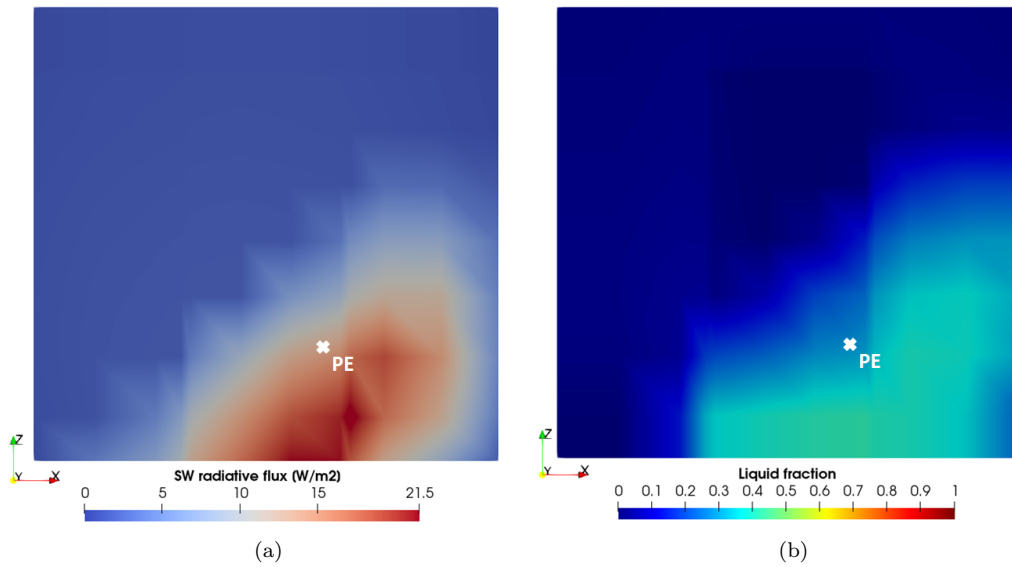


Figure 15: (a) Average SW heat flux distribution and (b) average liquid fraction distribution on the east wall in the superficial layer of *PCM2* in *C2* on the 14th of July 2013.

516 4.2.3. Interior wall heat fluxes

517 Figure 16 plots the evolution of interior heat fluxes for the east wall and
518 floor, comparing the results of $C1$ and $C2$ with those of $C0$ (the configura-
519 tion without the PCMs). The storage–release effect of the PCM discussed
520 in the previous subsections through β_{glob} and β_{loc} analysis is visible when
521 observing the evolution of the interior wall heat fluxes. The east wall in $C2$
522 absorbs up to 560 W for $PCM2$ when the sun patch passes over the wall;
523 the absorption is approximately 100 W more than that in the reference case
524 with no PCM. Similarly, the floor in $C1$ absorbs up to 500 W for $PCM2$, ap-
525 proximately 80 W more than the absorption in the reference case. The heat
526 is released throughout the night, and the magnitude of heat release is higher
527 in the configurations with the PCM. Moreover, it appears that $PCM2$ has
528 a marginally higher storage than $PCM1$, with similar release.
529 The impact of the storage–release effect of the PCM on the surface and op-
530 erative temperatures is evaluated in the following subsections.

531 4.2.4. Surface temperatures

532 Figures 17 and 18 plot the surface temperatures at specific locations by
533 comparing the results of $C1$ and $C2$ with those of $C0$. A surface temperature
534 decrease is observed owing to the latent heat storage of the PCMs. For the
535 probes receiving solar radiation, the decrease in the peak temperature during
536 the daytime reaches 3 °C in $C1$ at $PF - a$ and 6 °C in $C2$ at PE , and the
537 increase in the peak temperature during the nighttime is up to 1.8 °C in

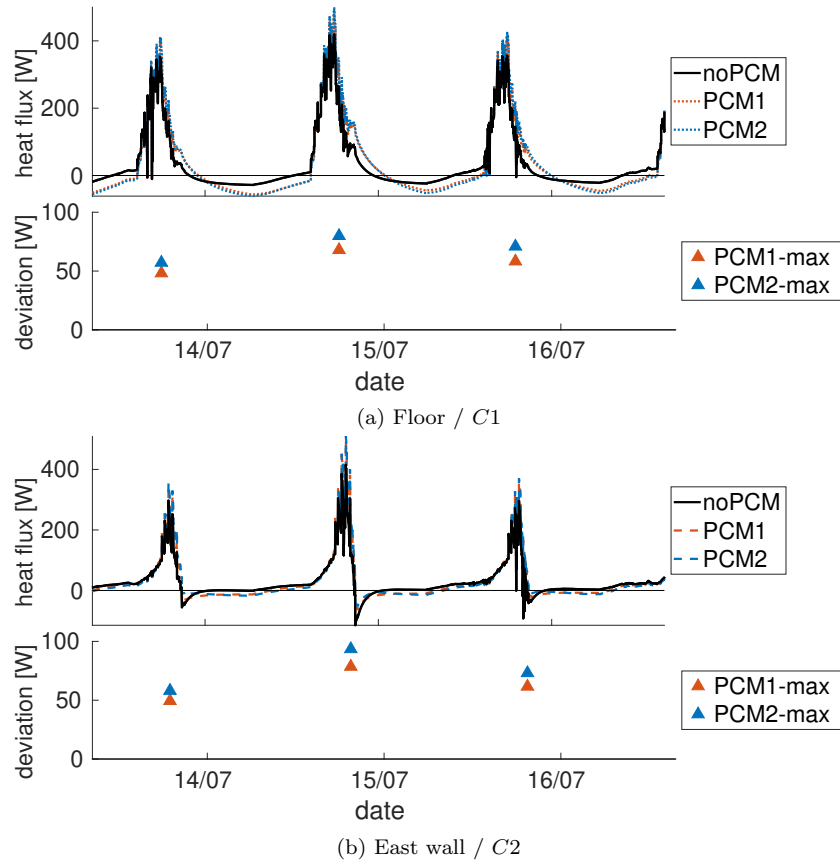


Figure 16: Interior wall heat fluxes and maximum peak heat flux deviation.

538 $C1$ and 0.9°C in $C2$. At the probes located outside the sun trajectory, the
 539 temperature fluctuation reduction is less significant but reaches 1.6°C in $C1$
 540 at $PF - a$ and 2.8°C in $C2$ at PE . In $C1$ and $C2$, both the PCMs exhibit
 541 similar surface temperature fluctuation reduction at the probes investigated.

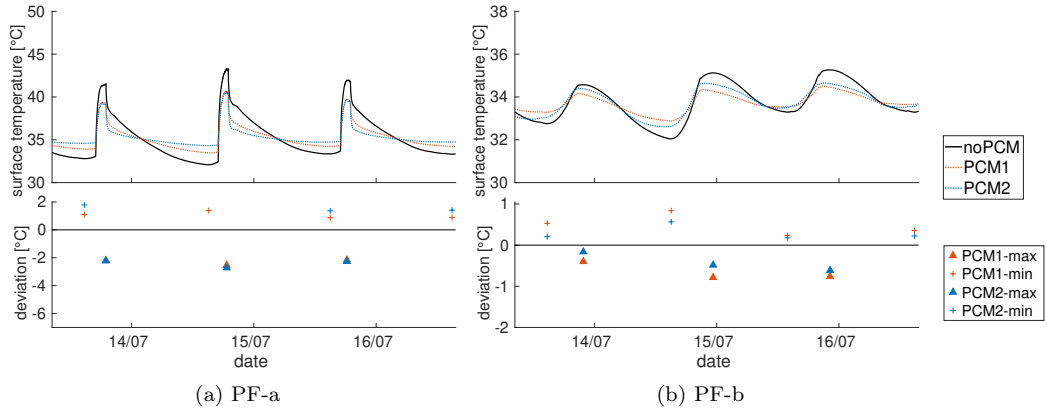


Figure 17: Surface temperatures and minimum and maximum peak temperature deviation in $C1$.

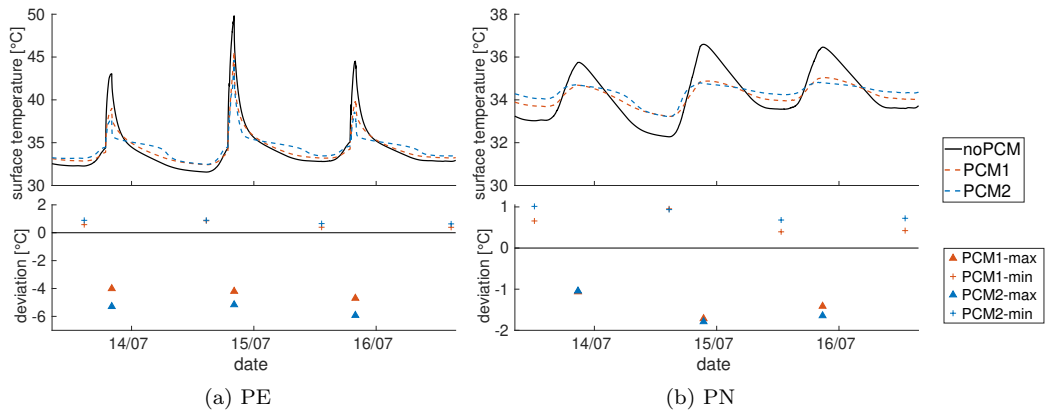


Figure 18: Surface temperatures and minimum and maximum peak temperature deviation in $C2$.

542 4.2.5. Operative temperature

543 The operative temperature is defined as the temperature of an isother-
544 mal enclosure in which an occupant exchanges the same amount of heat by
545 radiation and convection as in the enclosure in which the occupant is actu-
546 ally located. It considers the air temperature in the occupied zone and the
547 effects of radiation and indicates the thermal comfort in the room. Figure
548 19 shows the operative temperature evolution in the room in *C1* and *C2*
549 compared with that in *C0*. As expected, integrating PCM into the building
550 walls reduces the surface temperature and, consequently, the operative tem-
551 perature. During the daytime, the temperature decrease reaches 0.7°C in
552 *C1* with *PCM2* and 1.6°C in *C2* with *PCM2*, and the temperature increase
553 during the nighttime is up to 0.9°C in *C1* with *PCM1* and 1°C in *C2* with
554 *PCM1*. The temperature fluctuations are less significant in *C1* and *C2* than
555 in *C0*, with the smallest fluctuation range in *C2* of up to 2.6°C.
556 The study concludes that *PCM2* with a peak melting temperature of 35°C
557 and a narrow phase change temperature range integrated into the wall of
558 the BESTLab test cell, as in *C2* in the summer, is the most effective in the
559 mitigation of surface and operative temperature fluctuations.

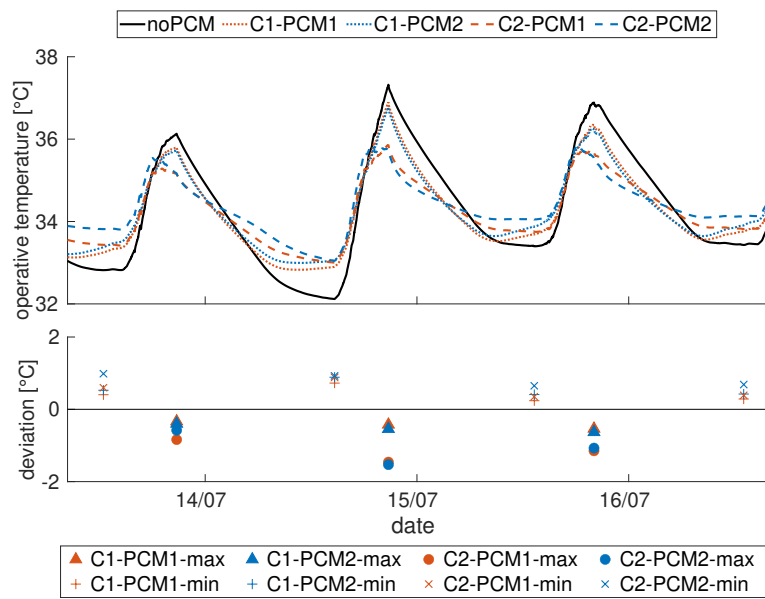


Figure 19: Operative temperature and maximum and minimum peak temperature deviation.

560 *4.3. Discussion*

561 The developed 3D and high-resolution dynamic thermal model is use-
562 ful for investigating the PCM's effectiveness and positioning optimization
563 considering the sun patch evolution in a well-insulated room. First, the 3D
564 description of the heat conduction in the building walls considers the thermal
565 bridge effects. Thus, the Psi values usually employed to account for thermal
566 bridges in the 1D models are no longer needed. These coefficients are a sub-
567 stantial source of error under dynamic conditions [35]. Second, the short
568 computational time-step enables capturing the rapid temperature variations
569 due to the sun patch. This induces abrupt changes in the local liquid frac-
570 tion distribution in the PCMs and wall heat fluxes. The model then enables
571 detailed optimization of the positioning and thickness of the PCM. In this
572 study, the base configuration is well-insulated, and the model considered the
573 asymmetric radiation heat transfer resulting from the sun patch evolution in
574 the room. It is beneficial to integrate the PCMs with the wall indoor sur-
575 faces to absorb the strong radiative fluxes and reduce the peak temperature.
576 The results show that in *C1*, which integrates a 22 mm thick PCM panel on
577 the floor, the latent heat is primarily stored in the first half-thickness of the
578 PCM (from *L1* to *L4*), and the storage declines sharply after *L4*. In *C2*,
579 which integrates a 7.6 mm thick PCM panel on the east, west, and south
580 walls, the liquid fraction is highly homogeneous throughout the PCM (from
581 *L1* to *L3*). Thus, the optimized thickness is approximately 10 mm for this
582 case. In addition, the results show a heterogeneous liquid fraction distribu-

583 tion in the PCM’s superficial layer; this is correlated to the SW heat flux
584 field in the room. This heterogeneity indicates that the latent heat is stored
585 primarily in parts of the PCM located on the sun patch, and the storage is
586 negligible elsewhere. Thus, the PCM integration could be limited to the sun
587 patch trajectory in the room to optimize its utilization and to limit the cost
588 of installation.

589 **5. Conclusions**

590 This study developed a 3D dynamic thermal model of a room for high-
591 resolution analysis of the heat transfer in the room walls, an improvement
592 over the typical building simulations. The model can handle a short compu-
593 tational time step of approximately a second to capture the dynamic thermal
594 effects and gives detailed surface temperature fields to account for highly het-
595 erogeneous thermal environments. Furthermore, the model can incorporate
596 windows to detect the sun patches in the room. The model was first vali-
597 dated without PCM using the BESTlab low-energy test cell equipped with
598 a window (experimentally investigated by Rodler [26]). A good agreement
599 between the simulation and experimental results was revealed with respect
600 to the room surface and air temperatures. In fact, the RMSE ranges between
601 0.42 to 0.74 confirming the accuracy of the model, although occasional dis-
602 crepancies in the temperature peaks up to 3.89°C are observed in the sun
603 patch.

604 The model was then applied to study the PCM efficiency and positioning

605 optimization in the BESTLab passive solar low-energy test cell during the
606 summer period using the effective heat capacity method. Two PCMs with
607 equal total enthalpy but different phase change temperature ranges were in-
608 tegrated as a panel on the floor (*C1*) and as panels on each of the walls that
609 face the window (*C2*). The results highlighted that the PCM with a narrow
610 phase change temperature range in *C2* was the most effective in reducing the
611 indoor temperature fluctuations; the peak surface temperature was reduced
612 by up to 6 °C in the sun patch, and the operative temperature fluctuations
613 were decreased by 2.6 °C. The model is relevant for evaluating the effective-
614 ness of the PCM and optimizing its positioning based on the detailed data on
615 the liquid fraction distributions in the PCMs, interior wall heat fluxes, and
616 surface temperature fields (that exhibit heterogeneity owing to the local and
617 dynamic evolution of the sun patch in the room). Such detailed information
618 would be useful in predicting thermal comfort in heterogeneous and dynamic
619 thermal environments.

620 The objective of this work is to demonstrate the capability of the developed
621 3D model to investigate the PCMs in a dynamic and heterogeneous ther-
622 mal environment rather than evaluate a realistic PCM in a complex build-
623 ing geometry. Consequently, an ideal PCM model has been implemented,
624 with its properties suited for use in this study. Usually, the PCM melting
625 temperature is below the thermal comfort temperature but above the night
626 temperature, and the night cooling should be sufficient to solidify the molten
627 material. Moreover, with its high spatial and temporal resolution, the model

628 can be used for detailed simulations of dynamic and non-uniform thermal
629 environments. However, the use of an explicit method to solve the governing
630 equations, although easier to implement than an implicit method, requires a
631 stability condition that constrains the time step, here to few seconds, and in-
632 duces a significant computation burden. Thus, the simulations are restricted
633 to periods of a few weeks prohibiting annual simulations of full scale building.
634 In addition, the inaccuracy of the explicit method for stiff problems might
635 be the cause of the observed deviations around the temperature peaks in the
636 sun patch. The implementation of an implicit or semi-implicit solution of
637 the governing equations could be considered to adress these issues.

638 Further studies could be conducted to analyze the behavior of realistic PCMs
639 in various building configurations and different periods, such as in winter or
640 in different climatic regions. The model predictions could also be compared
641 with the typical energy simulation programs to quantify the temperature
642 prediction improvements resulting from the model. In addition, the heat ca-
643 pacity function could be improved to consider the hysteresis or subcooling
644 characteristics of some PCMs. Moreover, the model is intended to be cou-
645 pled with CFD based on a Large Eddy Simulation. This coupling could lead
646 to significant improvements in the prediction of the convective heat transfer
647 coefficient, and the changes in the indoor airflow patterns owing to the PCM
648 could be analyzed. Also, the analysis of indoor thermal comfort dynam-
649 ics with realistic boundary conditions could be achieved with such a model
650 coupling.

651 **Declaration of Competing Interest**

652 The authors declare that they have no known competing financial inter-
653 ests or personal relationships that could have appeared to influence the work
654 reported in this paper.

655 **Acknowledgments**

656 The authors would like to thank Auline Rodler for providing data re-
657 garding the BESTLab test cell and for helpful advice. The authors would
658 like to acknowledge EDF (a part of "Buildings with High Energy Efficiency"
659 (BHEE) joint laboratory), which funded the experimental research carried
660 out on the BESTlab test cell.

661 **References**

- 662 [1] IEA, Tracking buildings, 2021.
- 663 [2] Q. Al-Yasiri, M. Szabó, Incorporation of phase change materials into
664 building envelope for thermal comfort and energy saving: A comprehen-
665 sive analysis, *Journal of Building Engineering* (2021).
- 666 [3] L. F. Cabeza, A. Castell, C. Barreneche, A. De Gracia, A. I. Fernández,
667 Materials used as PCM in thermal energy storage in buildings: A review,
668 *Renewable and Sustainable Energy Reviews* (2011).
- 669 [4] C. R. Swaminathan, V. R. Voller, On the Enthalpy Method, *Interna-*
670 *tional Journal of Numerical Methods for Heat Fluid Flow* (1993).

- 671 [5] V. Alexiades, A. D. Solomon, *Mathematical Modeling of Melting and*
672 *Freezing Processes*, Hemisphere Publishing Corporation, 1993.
- 673 [6] M. Costa, D. Buddhi, A. Oliva, Numerical simulation of a latent heat
674 thermal energy storage system with enhanced heat conduction, *Energy*
675 *Conversion and Management* (1998).
- 676 [7] H. T. Hashemi, C. M. Sliepcevich, A numerical method for solving two-
677 dimensional problems of heat conduction with change of phase, *Chem.*
678 *Eng. Prog. Symp. Series* (1967).
- 679 [8] S. R. Idelsohn, M. A. Storti, L. A. Crivelli, Numerical methods in phase-
680 change problems, *Archives of Computational Methods in Engineering*
681 (1994).
- 682 [9] V. R. Voller, An overview of numerical methods for solving phase change
683 problems, *Advances in numerical heat transfer* (1997).
- 684 [10] S. N. Al-Saadi, Z. Zhai, Modeling phase change materials embedded
685 in building enclosure: A review, *Renewable and Sustainable Energy*
686 *Reviews* (2013).
- 687 [11] B. Lamrani, K. Johannes, F. Kuznik, Phase change materials integrated
688 into building walls: An updated review, *Renewable and Sustainable*
689 *Energy Reviews* (2021).
- 690 [12] F. Kuznik, V. J., J. Noel, Optimization of a phase change material
691 wallboard for building use, *Applied Thermal Engineering* (2008).

- 692 [13] C. Voelker, O. Kornadt, M. Ostry, Temperature reduction due to the
693 application of phase change materials, *Energy and Buildings* (2008).
- 694 [14] X. Xu, Y. Zhang, K. Lin, H. Di, R. Yang, Modeling and simulation on
695 the thermal performance of shape-stabilized phase change material floor
696 used in passive solar buildings, *Energy and Buildings* (2005).
- 697 [15] J. Clarke, *Energy Simulation in Building Design* (2nd ed.), Butterworth-
698 Heinemann, London, 2001.
- 699 [16] Energyplus engineering reference, 2012.
- 700 [17] TRNSYS Mathematical Reference, Solar Energy Laboratory Madison,
701 UnitedStates, University of Wisconsin, 1996.
- 702 [18] G. Plessis, A. Kaemmerlen, A. Lindsay, Buildsyspro: a modelica library
703 for modelling buildings and energy systems, *Proceedings of the 10th*
704 *International Modelica Conference*, Lund, Sweden (2014).
- 705 [19] D. Heim, J. A. Clarke, Numerical modelling and thermal simulation of
706 PCM–gypsum composites with ESP-r, *Energy and Buildings* (2004).
- 707 [20] G. Evola, L. Marletta, F. Sicurella, Simulation of a ventilated cavity
708 to enhance the effectiveness of PCM wallboards for summer thermal
709 comfort in buildings, *Energy and Buildings* (2014).
- 710 [21] U. Stritih, V. V. Tyagi, R. Stropnik, H. Paksoy, F. Haghghat, M. M.

- 711 Joybari, Integration of passive PCM technologies for net-zero energy
712 buildings, *Sustainable Cities and Society* (2018).
- 713 [22] F. Kuznik, K. Johannes, E. Franquet, L. Zalewski, S. Gibout, P. Tit-
714 telein, J.-P. Dumas, D. David, J.-P. Bédécarrats, S. Lassue, Impact of
715 the enthalpy function on the simulation of a building with phase change
716 material wall, *Energy and Buildings* (2016).
- 717 [23] Ansys fluent user's guide, 2021.
- 718 [24] G. Diarce, Campos-Celador, K. Martin, A. Urresti, A. García-Romero,
719 J. Sala, A comparative study of the CFD modeling of a ventilated active
720 façade including phase change materials, *Applied Energy* (2014).
- 721 [25] B. Gowreesunker, S. Tassou, Effectiveness of CFD simulation for the
722 performance prediction of phase change building boards in the thermal
723 environment control of indoor spaces, *Building and Environment* (2013).
- 724 [26] A. Rodler, Modélisation dynamique tridimensionnelle avec tache solaire
725 pour la simulation du comportement thermique d'un bâtiment basse
726 consommation, Ph.D. thesis, INSA, Lyon, 2014.
- 727 [27] M. F. Cohen, S. E. Chen, J. R. Wallace, D. P. Greenberg, A progressive
728 refinement approach to fast radiosity image generation, *SIGGRAPH*
729 *Comput. Graph.* (1988).
- 730 [28] I. Ashdown, *Radiosity: A Programmer's Perspective*, Wiley, 2002.

- 731 [29] G. E. Alefeld, F. A. Potra, Y. Shi, Algorithm 748: enclosing zeros
732 of continuous functions, *ACM Transactions on Mathematical Software*
733 (1995).
- 734 [30] T. Blomberg, Heat conduction in two and three dimensions: computer
735 modelling of building physics applications, Ph.D. thesis, Lund Univer-
736 sity, 1996.
- 737 [31] S. Bontemps, A. Kaemmerlen, G. Blatman, L. Mora, Reliability of dy-
738 namic simulation models for building energy in the context of low-energy
739 buildings zonal models view project modelling for predictive control ap-
740 plication view project, In *Proceedings of the 13th Conference of Interna-*
741 *tional Building Performance Simulation Association*, Chambéry, France
742 (2013).
- 743 [32] W. H. McAdams, *Heat Transmission*, McGraw-Hill Kogakusha, 1954.
- 744 [33] H. B. Awbi, A. Hatton, Natural convection from heated room surfaces,
745 *Energy and Buildings* (1999).
- 746 [34] F. Kuznik, J. Virgone, J.-J. Roux, Energetic efficiency of room wall con-
747 taining PCM wallboard: A full-scale experimental investigation, *Energy*
748 *and Buildings* (2006).
- 749 [35] K. Martin, A. Erkoreka, I. Flores, M. Odriozola, J. M. Sala, Problems
750 in the calculation of thermal bridges in dynamic conditions, *Energy and*
751 *Buildings* (2011).